Photodissociation Dynamics of 2,5-Dihydroxyacetophenone

Yusuke Morisawa,[†] **Yuri A. Dyakov, Chien-Ming Tseng,**[‡] **Y. T. Lee,**[‡] **and Chi-Kung Ni***[,§]

Institute of Atomic and Molecular Sciences, Academia Sinica, P.O. Box 23-166, Taipei, 10617 Taiwan

Received: July 22, 2008; Revised Manuscript Received: October 21, 2008

Photodissociation of 2,5-dihydroxyacetophenone (DHAP), an important matrix compound in matrix-assisted laser desorption/ionization (MALDI), was studied in a molecular beam at 193 nm using multimass ion imaging techniques. Two major dissociation channels were observed, including (1) $C_6H_3(OH)_2COCH_3 \rightarrow OC_6H_3(OH)COCH_3 + H$ and (2) $C_6H_3(OH)_2COCH_3 \rightarrow C_6H_3(OH)_2 + COCH_3$. The minor channels include $C_6H_3(OH)_2COCH_3 \rightarrow C_6H_3(OH)_2CO + CH_3$ and/or $C_6H_3(OH)_2COCH_3 \rightarrow C_6H_3(OH)_2 + CO + CH_3$. The photofragment translational energy distribution suggests that reaction 1 occurs at an excited state in which the potential along the O−H bond distance is repulsive. Comparison to the branching ratios from RRKM calculations suggests that reaction 2 does not occur at either the ground state or the triplet state or that if it does occur at one of these states it must not follow the RRKM model. A comparison to the photodissociation dynamics of acetophenone and phenol and its derivatives was made.

I. Introduction

Ketones are known to dissociate efficiently via C−CO bond cleavage after UV excitaton.[1] Since the C−CO bond of an acyl radical is weak, acyl radicals formed with a sufficiently high internal energy may undergo further decomposition, producing CO and alkyl radicals. One example whose dissociation mechanism has been studied extensively is acetone.[2,3] Both acetyl (CH$_3$CO) and methyl (CH$_3$) radicals are observed in the 248 nm photodissociation of CH$_3$COCH$_3$, whereas only CO + 2CH$_3$ are identified to be products at 193 nm.

Acetophenone (C$_6$H$_5$COCH$_3$) is the simplest aromatic ketone. Early photochemical studies of acetophenone were motivated by the search for a convenient source of phenyl radicals.[4,5] The photodissociation of acetophenone at 193 and 248 nm has been studied using the time-of-flight mass spectrometric technique.[6] Two major primary channels, C$_6$H$_5$COCH$_3$ → C$_6$H$_5$CO + CH$_3$ and C$_6$H$_5$COCH$_3$ → C$_6$H$_5$ + COCH$_3$, were observed with comparable cross sections at the photolysis wavelength 193 nm. However, 30%−50% of primary C$_6$H$_5$CO and CH$_3$CO radicals further decompose, yielding secondary products C$_6$H$_5$ + CO and CH$_3$ + CO, respectively. At 248 nm, most of the acetophenone undergoes the first primary dissociation channel. A minor photodissociation channel, C$_6$H$_5$COCH$_3$ → C$_6$H$_5$CH$_3$ + CO, is identified at both 193 and 248 nm. Recent ultrafast electron diffraction study of acetophenone shows that it undergoes two channels upon excitation to S$_2$ by 266.7 nm.[7] Following femtosecond conversion to S$_1$, one channel leads to the dissociation products, benzoyl and methyl radicals, the other channel leads to intersystem crossing to the triplet state.

Compared to acetophenone, 2,5-dihydroxyacetophenone (DHAP, C$_6$H$_3$(OH)$_2$COCH$_3$) has a similar structure with two additional hydroxy groups. DHAP is frequently used as a matrix compound in matrix-assisted laser desorption/ionization (MAL-

DI).[8] MALDI is regularly used for peptide and protein analysis, but the details of mechanism are not understood. Several mechanisms have been proposed.[9] Photochemical ionization is one of the proposed MALDI mechanisms.[9a] In this mechanism, photoionization of matrix molecules is considered as the primary process for subsequent ionization of an analyte in the gas phase. However, several processes compete with photoionization after the irradiation of matrix compounds by UV photons. They include energy transfer and proton transfer between DHAP and multiphoton absorption followed by dissociation. Although DHAP is commonly used as the matrix compound for ultraviolet MALDI, the photochemistry of DHAP is not clear. In this work, we report the photodissociation of DHAP in a molecular beam by multimass ion imaging techniques. Results are compared to the photodissociation of acetophenone, phenol, and related compunds.

II. Experimental Section

The experimental techniques have been described in detail in our previous reports,[10−16] and only a brief account is given here. DHAP vapor was formed by flowing ultrapure He through a pulsed nozzle containing DHAP. The DHAP/He mixture was then expanded to form the molecular beam. Molecules in the molecular beam were photodissociated by 193 nm laser pulses, and fragments were ionized by vacuum ultraviolet (VUV) laser pulses. The distance and time delay between the VUV laser pulse and the photolysis laser pulse were set such that the VUV laser beam passed through the center of mass of the dissociation products and generated a line segment of photofragment ions through the center of mass of the dissociation products by photoionization. To separate the different masses within the ion segment, a pulsed electric field was used to extract the ions into a mass spectrometer after ionization. At the exit port of the mass spectrometer, a two-dimensional ion detector was used to detect the ion positions and intensity distribution; the mass-to-charge ratio and translational energy distributions for different fragments were measured simultaneously. In this ion image, one direction was the recoil velocity axis and the other direction

* Corresponding author. E-mail: ckni@po.iams.sinica.edu.tw.
† Present address: School of Science and Technology, Kwansei Gakuin University, 2-1 Gakuen Sanda 669-1337, Japan.
‡ Also at Department of Chemistry, National Taiwan University, Taipei, 10617, Taiwan.
§ Also at Department of Chemistry, National Tsing Hua University, Hsinchu, Taiwan.

was the mass axis. The image was accumulated for 0.1−0.5 million laser shots, according to the signal-to-noise ratio of the image.

Depending on the velocity of the molecular beam, it was necessary to change the distance between the photolysis laser beam and the VUV laser beam to match the delay time between these two laser pulses and to ensure that the ionization laser would pass through the center of mass of the products. The change of the distance between the two laser beams changed the length of the fragment ion segment in the image. The images were all in the line shape but with different lengths. However, if the molecules were not dissociated after the absorption of UV photons, these molecules contained high internal energy and would remain within the molecular beam. They flew with the same velocity (molecular beam velocity) to the ionization region and were ionized by the VUV laser. Dissociation occurred following the VUV photoionization for those hot molecules, which absorbed UV photons and did not dissociate into fragments before the arrival of the VUV laser beam. The shape of the image from the dissociative ionization was very different from that of the image from the dissociation products of neutral parent molecules. Since ionization and dissociation occurred at the same position, the image of dissociative ionization was a two-dimensional projection of the photofragment ion's three-dimensional recoil velocity distribution. It was a disk-like image, rather than a line-shape image. In addition, the size of the image from the dissociative ionization would not change with the delay time. On the other hand, if fragments cracked into small ionic species upon the VUV photoionization, the shape of the image was also disk-like, but the width of the image changed with the delay time. From the shape of the image and its change with the delay time, the images from the dissociation of neutral molecules, the dissociative ionization of undissociated excited molecules, and the fragment cracking can be easily distinguished.

Since the vapor pressure of DHAP is very low at room temperature, it is necessary to increase the temperature of the nozzle in order to increase the vapor pressure and therefore the concentration of DHAP in the molecular beam. However, DHAP was found to decompose easily at high temperature in a regular stainless steel nozzle. A special design of pulsed nozzle was made to generate a high concentration of DHAP in the molecular beam. A stainless steel oven maintained at 70 °C was attached to the front port of a pulse valve. The front surface of the nozzle was covered with a sheet of polyimide, and the inner surface of the oven was coated with graphite. The plunger of the pulsed valve made by polyimide was extended to the exit port of the oven to control the opening of the oven. DHAP mixed with graphite powder was loaded in the oven. Ultrapure He at a pressure of 400 Torr flowed from the nozzle to the oven. The sample/rare gas mixture was then expanded through the exit port of the oven to form the molecular beam. VUV photoionization and time-of-flight (TOF) mass spectrometry were used to check the content of the molecular beam before the photodissociation experiment was performed. Figure 1 shows the mass spectra obtained by VUV photoionization from the regular stainless steel nozzle and our special nozzle. It shows that only the parent mass of DHAP was observed from our special nozzle. On the other hand, grievous degradation of DHAP occurred inside the regular nozzle. It is likely that DHAP decomposed into toluene in the regular nozzle, according to the observation from the mass spectrum. However, further evidence is required to identify the structure of $m/e = 92$.
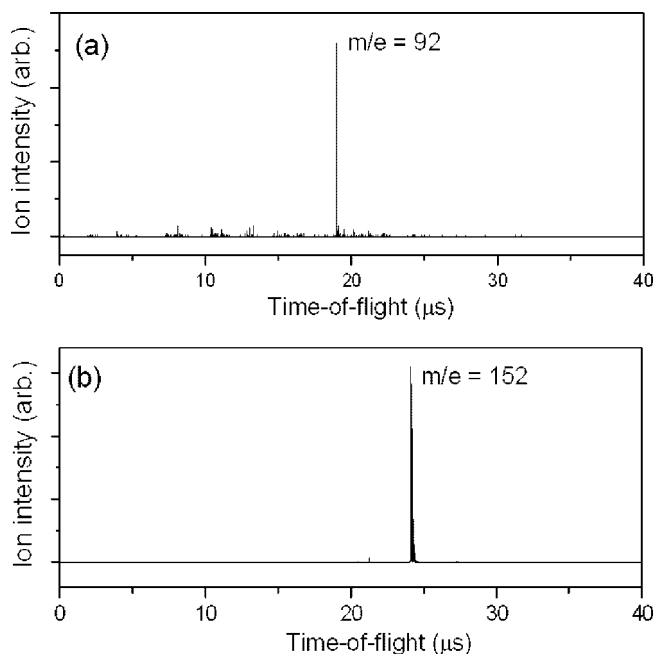

Figure 1. Time-of-flight mass spectra obtained from the 2,5-dihydroxyacetophenone ($m = 152$) molecular beam generated from (a) regular stainless steel valve and (b) specially designed valve. In addition to $m/e = 152$, its ^{13}C isotopes due to natural abundance were also observed. The photoionization wavelength is 118 nm.

III. Results and Discussion

Fragments of $m/e = 151, 136, 133, 109, 81, 43$, and 15 were observed from the photodissociation of DHAP at 193 nm using a 118 nm photoionization laser beam. Only fragments $m/e = 151, 109$, and 43 were observed using a 157 nm photoionization laser beam. Fragment ion intensities as a function of photolysis laser intensity were performed in the region of 0.26−2.1 mJ/cm^2, as illustrated in Figure 2. It shows that all the fragments result from one-photon dissociation.

A. H Atom Elimination Channel. The image of $m/e = 151$ is a line-shape image. It is the product from H atom elimination. The translational energy distribution for the H atom elimination channel is shown in Figure 3. Fragment H atom was not observed because the ionization energy of H atom is larger than the VUV photon energy we used in this experiment. The large translational energy release indicates that the dissociation occurs from a state at which the potential along the O−H bond distance is repulsive, or it is from a state with a large barrier in the exit channel. Since the generation of two radicals from the ground electronic state is not expected to have a large exit barrier, H atom elimination must occur from the excited state. Instead of the C−H bond in the alkyl group or aromatic ring, O−H is the electronic chromophore at 193 nm and the H atom elimination must result from the following reaction: $C_6H_3(OH)_2COCH_3$ ($m = 152$) → $OC_6H_3(OH)COCH_3$ ($m = 151$) + H.

The velocity distributions of fragments $m/e = 136$ and $m/e = 133$ were found to be very similar to that of $m/e = 151$. This suggests that both $m/e = 136$ and $m/e = 133$ result from dissociative ionization of fragment $m = 151$ by VUV photoionization due to excess VUV photon energy: $OC_6H_3(OH)COCH_3$ ($m = 151$) + $h\nu$ (118 nm) → $OC_6H_3(OH)CO^+$ ($m = 136$) + CH_3 or $C_8H_5O_2^+$ ($m = 133$) + H_2O.

The other possible explanation for $m/e = 136$ is that it results from CH_4 elimination: $C_6H_3(OH)_2COCH_3$ → $C_7H_4O_3$ ($m = 136$) + CH_4. Although we are not able to detect CH_4 due to its high

Photodissociation Dynamics of DHAP

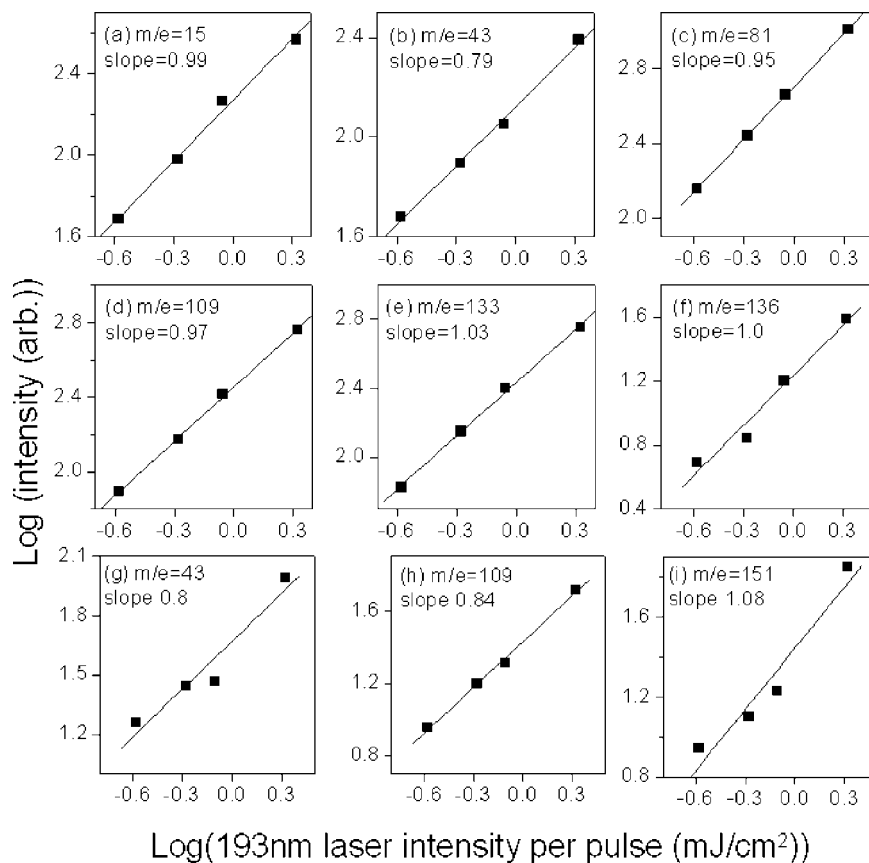*J. Phys. Chem. A, Vol. 113, No. 1, 2009* **99**

Figure 2. Fragment ion intensity as a function of 193 nm photolysis laser intensity. VUV wavelength is 118 nm for (a)−(f) and 157 nm for (g)−(i). The slopes are all very close to 1, indicating one-photon dissociation.
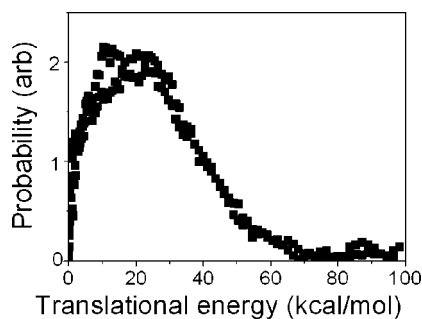

Figure 3. Fragment translational energy distribution for reaction $C_6H_3(OH)_2COCH_3 \rightarrow C_6H_3(OH)(O)COCH_3 + H$. The translational energy is displayed in center-of-mass frame. The VUV wavelength is 157 nm.

ionization potential, the following argument allowed us to eliminate this channel. The peak of the total translational energy distribution is located at 1.4 kcal/mol, and the maximum value of translational energy is only 4 kcal/mol if $m/e = 136$ is from the CH_4 elimination. Since the heat of reaction for CH_4 elimination is only 34.8 kcal/mol and the available energy is as large as 120 kcal/mol, the peak and maximum values of the translational energy observed from $m/e = 136$ are too small to assume that $m/e = 136$ is from CH_4 elimination. A similar argument can be applied to fragment $m/e = 133$. If fragment $m/e = 133$ comes from $m = 134$ (the heavy fragment of H_2O loss channel) due to the cracking upon ionization, then the peak and maximum values of the fragment translational energy are only 1.2 and 3.5 kcal/mol, respectively. They are too small for the channel with such a small heat of reaction ($\Delta H = 78$ kcal/mol for $C_6H_3(OH)_2COCH_3 \rightarrow C_8H_6O_2$ ($m = 134$) + H_2O).

B. COCH₃ and CH₃ Elimination Channels. For the rest of fragments $m/e = 109$, 81, 43, and 15, the following analysis shows that they must result from the major channel $C_6H_3(OH)_2COCH_3 \rightarrow C_6H_3(OH)_2$ ($m = 109$) + $COCH_3$ ($m = 43$) and the minor channels $C_6H_3(OH)_2COCH_3 \rightarrow C_6H_3(OH)_2CO$ ($m = 137$) + CH_3 ($m = 15$) and/or $C_6H_3(OH)_2COCH_3 \rightarrow C_6H_3(OH)_2$ ($m = 109$) + CO ($m = 28$) + CH_3 ($m = 15$). Due to the large ionization energy of CO molecules, we cannot observe CO fragments. Both $m/e = 109$ and $m/e = 43$ have line-shape images, corresponding to the dissociation channel: $C_6H_3(OH)_2COCH_3 \rightarrow C_6H_3(OH)_2$ ($m = 109$) + $COCH_3$ ($m = 43$). However, comparison of the momentum distributions of these two fragments shows there is a small difference between them. For example, if they match in the high momentum region, then the momentum distribution of $m/e = 109$ has a smaller intensity in the low momentum region, as shown in Figure 4a. One possibility is that some of the fragments $m = 109$ with larger internal energy dissociate into smaller fragments upon ionization. On the other hand, the image of fragment $m/e = 81$ is disk-like, but the width of the image changes with the pump−probe delay time, indicating that $m/e = 81$ results from the dissociative ionization of heavy fragments. Indeed, the momentum distribution of $m/e = 81$ is very similar to that of $m/e = 109$ if we use a mass value of 109 in the calculation of $m/e = 81$ momentum distribution, as shown in Figure 4a. This suggests that $m/e = 81$ is from the dissociative ionization (cracking) of fragment $m = 109$ by VUV photoionization due to the excess VUV photon energy. Our calculation, as shown in Table 1, also supports that fragment $m = 109$ can easily crack into a smaller ionic fragment $m/e = 81$ after 118 nm photoionization. The momentum distribution difference between $m/e = 109$ and $m/e = 81$ must be caused by the cracking efficiency
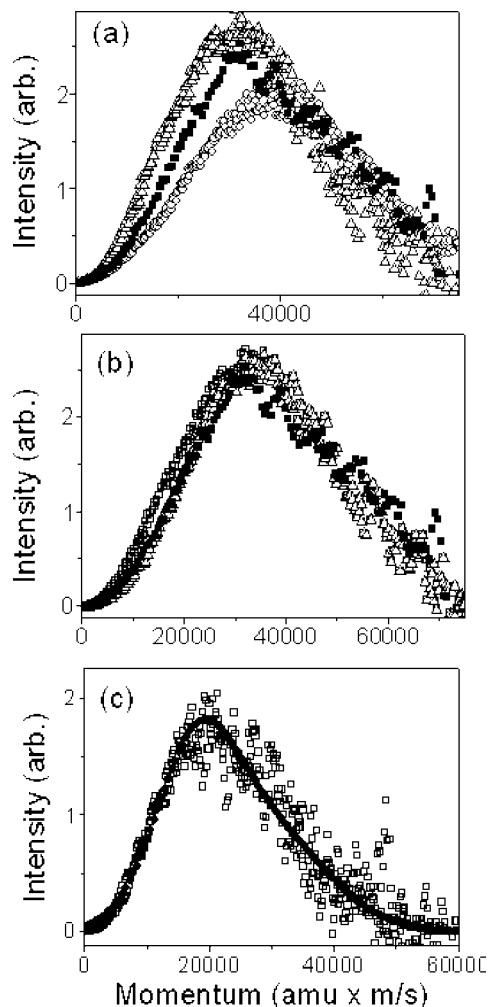
Figure 4. Fragment momentum distribution for (a) $m/e = 43$ (solid squares), 81 (open triangles), and 109 (open circles); (b) $m/e = 43$ (solid squares), sum of $m/e = 81$ and 109 (open squares), and sum of $m/e = 81$ and 109 after subtraction of small fraction of $m/e = 109$ (open triangles); and (c) $m/e = 15$ (solid squares) and $m/e = 137$ (from the small fraction of $m/e = 109$, open squares). The momentum distribution is displayed in center-of-mass frame. Ions were obtained by 118 nm photoionization, except $m/e = 43$ obtained by 157 nm.

difference of $m/e = 109$ with different internal energy. Fragments with large internal energy (therefore small momentum) are easier to crack into smaller ionic fragments. As a result, the intensity of $m/e = 81$ is larger than that of $m/e = 109$ in the low momentum region. The sum of the momentum distributions of $m/e = 81$ and $m/e = 109$ is very close to the momentum distribution of $m/e = 43$, except the intensity of $m/e = 43$ now becomes a little smaller than the sum of $m/e = 109$ and $m/e = 81$ momentum distributions in the low momentum region, as shown in Figure 4b.

The observation of the line-shape image for $m/e = 15$ without the corresponding heavy fragment partner $m/e = 137$ suggests two possibilities. First, fragment $m = 15$ may come from the secondary dissociation of the fragment $COCH_3$ ($m = 43$) with large internal energy (i.e., slow velocity): $COCH_3$ ($m = 43$) → $CO + CH_3$ ($m = 15$). This can explain why the momentum distribution of $m/e = 43$ is a little smaller than the sum of $m/e = 109$ and $m/e = 81$ momentum distributions in the low momentum region. After the secondary dissociation, the velocity of fragment CH_3 may change a lot from the initial $COCH_3$ velocity due to the small mass of CH_3 compared to CO. For such a three-body dissociation, it is difficult to verify the

secondary dissociation from simple momentum distributions, i.e., comparison of the momentum distribution between the sum of CH_3 (use $m = 43$ in momentum calculation) and $COCH_3$ and the sum of $m/e = 81$ (use $m = 109$ in momentum calculation) and $m/e = 109$.

The second possibility is that the heavy fragment partner $m = 137$ undergoes secondary dissociation into $m = 109$ and $m = 28$ completely. Since the mass of 109 is much larger than the mass of 28, the velocity of $m = 109$ does not change very much from that of $m = 137$ after the secondary dissociation. For such a three-body dissociation, the secondary dissociation process can be verified by the simple momentum match. Since the momentum distributions of $m = 109$ (use $m = 137$ in momentum calculation) and momentum distributions of $m/e = 15$ are very different, it indicates that most of $m = 109$ does not result from $m = 137$ due to the secondary dissociation. Therefore, the amount of mass 109 that results from the fragment $m = 137$ is small. On the other hand, the momentum distribution of $m = 109$ and $m = 43$ are very close, suggesting most of $m = 109$ comes from $C_6H_3(OH)_2COCH_3$ → $C_6H_3(OH)_2$ ($m = 109$) + $COCH_3$ ($m = 43$). If we take a small fraction of the momentum distribution from $m/e = 109$ and use $m = 137$ in the momentum calculation to match with that of $m/e = 15$, as illustrated in Figure 4c, then the sum of the momentum distribution of $m/e = 81$ and the rest of the momentum distribution of $m/e = 109$ matches very well with that of $m/e = 43$, as illustrated in Figure 4b. This indicates the minor channel $C_6H_3(OH)_2COCH_3$ → $C_6H_3(OH)_2CO$ ($m = 137$) + CH_3 ($m = 15$), and the heavy fragment undergoes secondary dissociation $C_6H_3(OH)_2CO$ ($m = 137$) → $C_6H_3(OH)_2$ ($m = 109$) + CO ($m = 28$).

In summary, fragment $m = 109$ comes from the major channel $C_6H_3(OH)_2COCH_3$ → $C_6H_3(OH)_2$ ($m = 109$) + $COCH_3$ ($m = 43$). Fragment CH_3 mainly results from the minor channel $C_6H_3(OH)_2COCH_3$ → $C_6H_3(OH)_2CO$ ($m = 137$) + CH_3 ($m = 15$) or the minor secondary dissociation channel $COCH_3$ ($m = 43$) → CO ($m = 28$) + CH_3 ($m = 15$). Ion $m/e = 81$ results from fragment cracking upon ionization, $C_6H_3(OH)_2$ ($m = 109$) + $h\nu$ (VUV) → $C_5H_4OH^+$ ($m/e = 81$) + CO, and heavy fragment $m = 137$ undergoes secondary dissociation, $C_6H_3(OH)_2CO$ ($m = 137$) → $C_6H_3(OH)_2$ ($m = 109$) + CO ($m = 28$). The translational energy distributions for these dissociation channels are illustrated in Figure 5.

C. Theoretical Calculations. We used ab initio methods to calculate geometries and energies of various transition states and dissociation products in the ground electronic state and triplet state. In the calculations, the geometries were optimized at the hybrid density functional B3LYP/6-31G* level, and the energies were calculated using a G3 model chemistry scheme. In addition, RRKM calculations of energy-dependent reaction rate constants were performed for most relevant dissociation processes. The dissociation barriers, thresholds, and branching ratios from calculations are listed in Table 1.

All the simple bond fission dissociation channels that generate two radicals, including H, OH, CH_3, and $COCH_3$ eliminations, do not have exit barriers, or very small barriers from molecular structure geometric relaxation. The calculations show that H atom elimination channels have dissociation thresholds in the region of 116.8−84.6 kcal/mol, depending on the position of the H atom. The H atom eliminations from the hydroxyl groups have low dissociation thresholds, and H atom eliminations directly from the aromatic ring have high thresholds. OH eliminations also have high thresholds, but the thresholds for CH_3 and $COCH_3$ eliminations are low. All the dissociation

Photodissociation Dynamics of DHAP

J. Phys. Chem. A, Vol. 113, No. 1, 2009 **101**

TABLE 1: Reaction Barrier Heights, Heat of Reactions, and Branching Ratios[a]

reactions	barriers	ΔH	branching ratios[b]
S_0 (0)			
$C_6H_3(OH)_2COCH_3 \rightarrow C_6H_2(OH)_2COCH_3 + H$		113.7−116.8	
$C_6H_3(OH)_2COCH_3 \rightarrow C_6H_3(OH)_2COCH_2 + H$		98.2	
$C_6H_3(OH)_2COCH_3 \rightarrow C_6H_3(OH)(O)COCH_3 + H$	84.6−91.8	94.0−90.2	
$C_6H_3(OH)_2COCH_3 \rightarrow C_6H_3(OH)_2CO + CH_3$		73.6	19
$C_6H_3(OH)_2COCH_3 \rightarrow C_6H_3(OH)_2 + COCH_3$		106.8	
$C_6H_3(OH)_2COCH_3 \rightarrow C_6H_3(OH)(O)CO + CH_4$	67.7	34.8	81
$C_6H_3(OH)_2COCH_3 \rightarrow C_6H_2(OH)COCH_3 + H_2O$	87.3	72.3	
$C_6H_3(OH)_2COCH_3 \rightarrow C_6H_4(OH)CH_3 + CO$	98.7	7.6	
$C_6H_3(OH)_2COCH_3 \rightarrow C_6H_4(OH)COCH_3 + OH$		110.7−119.6	
T_1 (70.7)			
$C_6H_3(OH)_2COCH_3 \rightarrow C_6H_3(OH)_2COCH_3 + CH_3$	98.3	73.6	99
$C_6H_3(OH)_2COCH_3 \rightarrow C_6H_3(OH)_2 + COLH_3$	109.4	106.8	1
Fragment Cracking			
$COCH_3 \rightarrow CO + CH_3$		6.4	14.8
$C_6H_3(OH)_2 \rightarrow C_6H_3(OH)_2^+$		192.9[c]	
$C_6H_3(OH)_2^+ \rightarrow$ cyclic $C_5H_4OH^+ + CO$	26.9	−30.9	

[a] Energies in units of kcal/mol. [b] Branching ratios are calculated using RRKM method for S_0 and T_1 separately. [c] Vertical ionization potential.
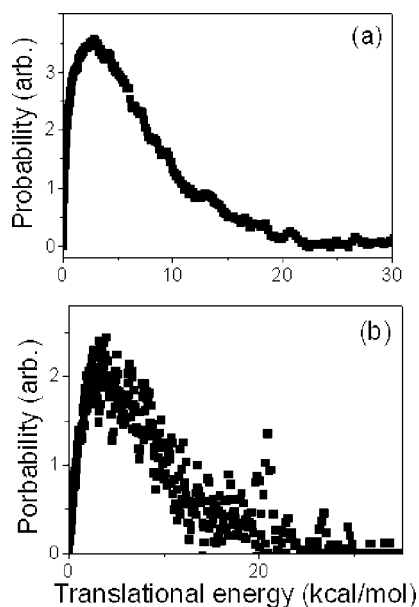

Figure 5. Fragment translational energy distribution for reactions (a) $C_6H_3(OH)_2COCH_3 \rightarrow C_6H_3(OH)_2 + COCH_3$ and (b) $C_6H_3(OH)_2COCH_3 \rightarrow C_6H_3(OH)_2CO + CH_3$. The translational energy is displayed in center-of-mass frame.

channels that generate two closed shell molecules have high barriers, but small heats of reaction. The RRKM calculations show that the ground state dissociation is dominated by CH_4 elimination due to the lowest dissociation barrier. A small amount of CH_3 elimination also occurs. This is not consistent with our experimental observation. On the other hand, the triplet state dissociation mainly includes two dissociation channels, i.e., CH_3 elimination and $COCH_3$ elimination. However, the branching ratios still do not agree with our experimental measurement very well. This suggests that the dissociation does not occur on either the ground state or the triplet state, or that the dissociation does not follow the statistical dissociation rate. At this moment, we do not have further evidence to show how the dissociation actually occurs.

On the other hand, theoretical calculations do support the possible secondary dissociation channels. Calculation indicates that the dissociation barrier for the secondary dissociation $COCH_3 \rightarrow CO + CH_3$ is only 14.8 kcal/mol. Since the dissociation energy for the primary dissociation $C_6H_3(OH)_2COCH_3 \rightarrow C_6H_3(OH)_2 + COCH_3$ is only 106.8 kcal/mol, the available energy (E(193 nm) − 106.8 = 41.3 kcal/mol) is more than enough for fragments to undergo secondary dissociation. A similar situation occurs in $C_6H_3(OH)_2COCH_3 \rightarrow C_6H_3(OH)_2CO + CH_3$. The dissociation energy is only 73.6 kcal/mol. The barrier of the secondary dissociation $C_6H_3(OH)_2CO \rightarrow C_6H_3(OH)_2 + CO$ is only 27 kcal/mol. Therefore, the fragment $C_6H_3(OH)_2CO$ (m = 137) generated with the available energy of 74.5 kcal/mol can easily dissociate into smaller fragments $C_6H_3(OH)_2 + CO$.

D. Comparison to Phenol, *p*-Methylphenol, *p*-Ethylphenol, *p*-(2-Aminoethyl)phenol, and Acetophenone. Recent ab initio calculations[17−19] suggest that the low fluorescence quantum yield of phenol is due to the dissociative character of the electronic excited state potential energy surface, instead of fast internal conversion to the electronic ground state. These calculations show that absorption of UV photons at 290−240 nm corresponds to the photoexcitation of phenol to the S_1 $\pi\pi^*$ excited state. The second excited state has a significant antibonding σ^* character with respect to the OH bond distance. The population of the bright state, S_1, can be transferred to the dark state, S_2, through a conical intersection. As a result, instead of internal conversion to the ground electronic state, predissociation through $\pi\pi^*$ and $\pi\sigma^*$ coupling results in rapid quenching of the fluorescence. Indeed, the H atom elimination from the repulsive electronic excited state of phenol has been verified in a recent molecular beam experiment.[20−22] H atom elimination was also found in the photodissociation of *p*-methylphenol and *p*-ethylphenol.[23] The photofragment translational energy distributions and potential energy surfaces from ab initio calculations suggest that H atom elimination occurs from a repulsive excited state. On the other hand, the H atom elimination channel is quenched completely by internal conversion and/or intersystem crossing in *p*-(2-aminoethyl)phenol. Only C−C bond cleavage was observed from *p*-(2-aminoethyl)phenol.[23] However, these side-chain size-dependent dissociation properties were not found in the photodissociation of DHAP. H atom elimination from the repulsive excited state still remains as one of the primary dissociation channels in DHAP.

On the other hand, ketone dissociation character, i.e., C−CO bond cleavage, still plays an important role in the dissociation process. The major channel is $C_6H_3(OH)_2COCH_3 \rightarrow C_6H_3(OH)_2 + COCH_3$. The minor channel is $C_6H_3(OH)_2COCH_3 \rightarrow C_6H_3(OH)_2CO + CH_3$, or three-body dissociation $C_6H_3(OH)_2COCH_3 \rightarrow C_6H_3(OH)_2 + COCH_3 \rightarrow C_6H_3(OH)_2 + CO + CH_3$. The result suggests bifurcation in the excited state. One possibility is predissociation through $\pi\pi^*$ and $\pi\sigma^*$ coupling, resulting in H atom elimination. The other possibility is the internal conversion and/or intersystem crossing to the lower states and eventually C−CO bond cleavage occurs.

References and Notes

(1) Calvert, J. G.; Pitts, J. N. *Photochemistry*; Wiley: New York, 1966.

(2) North, S. W.; Blank, D. A.; Gezelter, J. D.; Longfellow, C. A.; Lee, Y. T. *J. Chem. Phys.* **1995**, *102*, 4447.

(3) Kim, S. K.; Pederson, S.; Zewail, A. H. *J. Chem. Phys.* **1995**, *103*, 477.

(4) Glazebrook, H. H.; Pearson, T. G. *J. Chem. Soc.* **1939**, 589.

(5) Duncan, F. J.; Trotman-Dickenson, A. F. *J. Chem. Soc.* **1962**, 4672.

(6) Zhao, H. Q.; Cheung, Y. S.; Liao, C. L.; Liao, C. X.; Ng, C. Y.; Li, W. K. *J. Chem. Phys.* **1997**, *107*, 7230.

(7) Park, S. T.; Feenstra, J. S.; Zewail, A. H. *J. Chem. Phys.* **2006**, *124*, 174707.

(8) Krause, J.; Stoeckli, M.; Schlunegger, U. P. *Rapid Commun. Mass Spectrom.* **1996**, *10*, 1927.

(9) (a) Ehring, H.; Karas, M.; Hillenkamp, F. *Org. Mass Spectrom.* **1992**, *27*, 427. (b) Karas, M.; Kruger, R. *Chem. Rev.* **2003**, *103*, 427. (c) Chang, W. C.; Huang, L. C. L.; Wang, Y. S.; Peng, W. P.; Chang, H. C.; Hsu, N. Y.; Yang, W. B.; Chen, C. H. *Anal. Chim. Acta* **2007**, *582*, 1.

(10) Tsai, S. T.; Lin, C. K.; Lee, Y. T.; Ni, C. K. *J. Chem. Phys.* **2000**, *113*, 67.

(11) Tsai, S. T.; Huang, C. L.; Lee, Y. T.; Ni, C. K. *J. Chem. Phys.* **2001**, *115*, 2449.

(12) Tsai, S. T.; Lin, C. K.; Lee, Y. T.; Ni, C. K. *Rev. Sci. Instrum.* **2001**, *72*, 1963.

(13) Lin, C. K.; Huang, C. L.; Jiang, J. C.; Chang, H.; Lin, S. H.; Lee, Y. T.; Ni, C. K. *J. Am. Chem. Soc.* **2002**, *124*, 4068.

(14) Huang, C. L.; Jiang, J. C.; Mebel, A. M.; Lee, Y. T.; Ni, C. K. *J. Am. Chem. Soc.* **2003**, *125*, 9814.

(15) Ni, C. K.; Lee, Y. T. *Int. Rev. Phys. Chem.* **2004**, *23*, 187.

(16) Ni, C. K.; Tseng, C. M.; Lin, M. F.; Dyakov, Y. *J. Phys. Chem. B* **2007**, *111*, 12631.

(17) Sobolewski, A. L.; Domcke, W.; Dedonder-Lardeuxc, C.; Jouvet, C. *Phys. Chem. Chem. Phys.* **2002**, *4*, 1093.

(18) Lan, Z.; Domcke, W.; Vallet, V.; Sobolewski, A. L.; Mahapatra, S. *J. Chem. Phys.* **2005**, *122*, 224315.

(19) Sobolewski, A. L.; Domcke, W. *J. Phys. Chem. A* **2001**, *105*, 9275.

(20) Tseng, C. M.; Lee, Y. T.; Ni, C. K. *J. Chem. Phys.* **2004**, *121*, 2459.

(21) Nix, M. G. D.; Devine, A. L.; Cronin, B.; Dixon, R. N.; Ashfold, M. N. R. *J. Chem. Phys.* **2006**, *125*, 133318.

(22) Tseng, C. M.; Lee, Y. T.; Lin, M. F.; Ni, C. K.; Liu, S. Y.; Lee, Y. P.; Xu, Z. F.; Lin, M. C. *J. Phys. Chem. A* **2007**, *111*, 9463.

(23) Tseng, C. M.; Lee, Y. T.; Ni, C. K.; Chang, J. L. *J. Phys. Chem. A* **2007**, *111*, 6674.